

TOWARDS INTERPRETABLE VISUAL DECODING WITH ATTENTION TO BRAIN REPRESENTATIONS

Pinyuan Feng^{1*} Hossein Adeli¹ Wenxuan Guo¹

Fan Cheng¹ Ethan Hwang¹ Nikolaus Kriegeskorte¹

¹Zuckerman Mind Brain Behavior Institute, Columbia University, New York, USA

ABSTRACT

Recent work has demonstrated that complex visual stimuli can be decoded from human brain activity using deep generative models, helping brain science researchers interpret how the brain represents real-world scenes. However, most current approaches leverage mapping brain signals into intermediate image or text feature spaces before guiding the generative process, masking the effect of contributions from different brain areas on the final reconstruction output. In this work, we propose *NeuroAdapter*, a visual decoding framework that directly conditions a latent diffusion model on brain representations, bypassing the need for intermediate feature spaces. Our method demonstrates competitive visual reconstruction quality on public fMRI datasets compared to prior work, while providing greater transparency into how brain signals shape the generation process. To this end, we contribute an Image–Brain BI-directional interpretability framework (*IBBI*) which investigates cross-attention mechanisms across diffusion denoising steps to reveal how different cortical areas influence the unfolding generative trajectory. Our results highlight the potential of end-to-end brain-to-image decoding and establish a path toward interpreting diffusion models through the lens of visual neuroscience.

1 INTRODUCTION

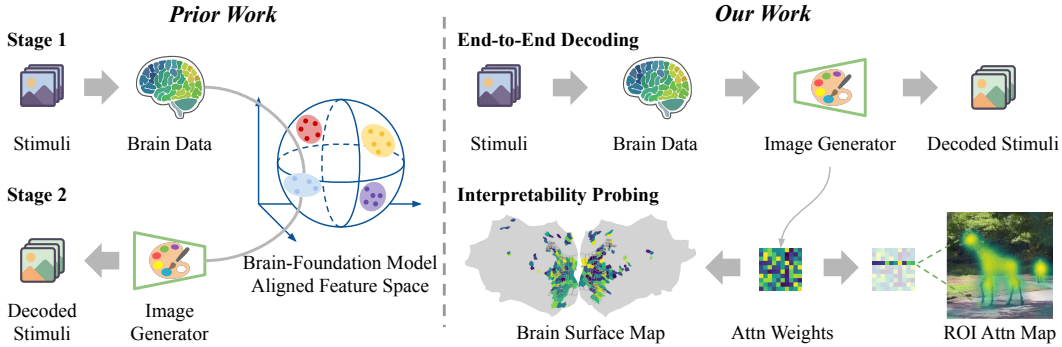


Figure 1: **Overview.** *Left:* Typical two-stage decoding pipelines first map brain activity to intermediate feature spaces (e.g., CLIP/DINO) and then use those embeddings to guide a generative model. *Right:* Our end-to-end approach conditions a latent diffusion model directly on brain activity, enabling interpretations of the generative dynamics in both image and brain spaces.

Understanding how the human brain represents the visual world remains a profound scientific problem in neuroscience. The decoding studies can address this challenge by revealing the content of the representation in different brain areas or the whole brain in response to complex stimuli. Recent years have witnessed the remarkable success in models decoding different perceptual modalities and

*pf2477@columbia.edu

intended movements from the brain with many of these models leveraging deep generative models in their pipeline. These works have pushed the NeuroAI frontier of decoding "thoughts" from brain activity, bringing the prospect of "mind reading" closer to reality.

Current approaches to reconstructing visual stimuli from brain activity (Lin et al., 2022; Cheng et al., 2023; Takagi & Nishimoto, 2023; Ozcelik & VanRullen, 2023; Scotti et al., 2023; Li et al., 2025) typically implement a two-stage pipeline (Fig. 1, left): (i) brain activity is first mapped to intermediate image- or text- embeddings derived from large foundation models (e.g. CLIP (Radford et al., 2021) and DINO (Caron et al., 2021; Oquab et al., 2023; Siméoni et al., 2025)); (ii) these intermediate representations are then used to condition a visual generative model for stimulus reconstruction. Mapping brain data into an intermediate representation space leverages rich priors in embedding spaces to improve reconstruction quality and has proved highly effective for reconstruction. However, the use of this intermediate representation can introduce an information bottleneck (Mayo et al. (2024)) with successful reconstruction of perceived stimuli depending on the alignment between neural representations and the embedding space. This intermediate step can also mask the effect of different brain areas and their content on the final reconstruction limiting the interpretability of the approach. In this work, we explore an alternative (Fig. 1, right) to two-stage decoding pipelines by conditioning latent diffusion models directly on the brain activity.

Contributions of our paper. Our contributions are as follows: (1) we propose *NeuroAdapter*, an end-to-end framework that learns parcel-wise embeddings from fMRI data and integrates them into latent diffusion models through cross-attention; (2) we show that our approach achieves competitive performance on public fMRI datasets, demonstrating that high-quality visual reconstructions can be obtained without reliance on external embedding spaces; and (3) we provide a bi-directional interpretability framework, namely *IBBI*, which leverages cross-attention dynamics across diffusion steps to reveal both the relative contribution of brain parcels and their spatial influence in the reconstructed images, offering new insights into the generative process from a neuroscientific perspective.

2 RELATED WORK

Brain Decoding with Deep Generative Models. With the rise of deep generative modeling, decoding has progressed from simple classification to photorealistic reconstructions that leverage powerful image priors. Early GAN-based pipelines established the feasibility of mapping brain signals into deep feature spaces and synthesizing images (Seeliger et al., 2018; Shen et al., 2019a;b; Cheng et al., 2023; Gu et al., 2024). Latent diffusion has since become the dominant image prior, with several methods steering Stable Diffusion via fMRI-predicted image/text latents (Lin et al., 2022; Chen et al., 2023; Ozcelik & VanRullen, 2023; Scotti et al., 2023; Takagi & Nishimoto, 2023; Zeng et al., 2024). Contemporary systems extend this recipe with different controllers and training regimes (Xia et al., 2024; Han et al., 2024; Huo et al., 2024; Li et al., 2025); and cross-subject generalization (Scotti et al., 2024; Wang et al., 2024; Gong et al., 2025). Despite this progress, most pipelines still route brain activity through intermediate vision or vision-language feature bottlenecks to guide generations, a design choice our *NeuroAdapter* method avoids by conditioning the latent diffusion model directly on brain representations in order to make the process more Interpretable.

Interpretable Visual Decoding. Different approaches have been developed to interpret the performance of and extract neuroscientific insights from the image decoding models. Some studies have examined how specific cortical areas affect reconstructions by training and testing on subsets of visual cortex areas (Shen et al., 2019a;b; Cheng et al., 2023; Ozcelik & VanRullen, 2023). Other methods have looked into the representations of the latent diffusion models to examine when (diffusion steps) and where (model layer) low- and high-level image features emerge (Takagi & Nishimoto, 2023). However, these approaches typically lack an explicit time-resolved view of which parts of the generated image are affected by brain signals. Our work addresses this exact gap by building a more interpretable pipeline using the cross-attention mechanism.

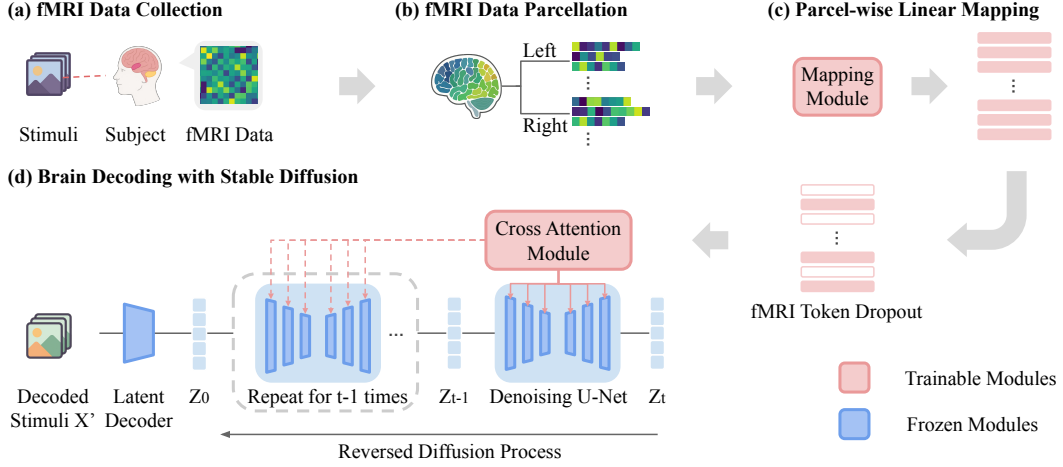


Figure 2: **NeuroAdapter training pipeline.** (a) fMRI data collection paradigm, (b) cortical parcellation, (c) parcel-wise linear mapping from vertices to brain representation tokens, and (d) conditioning a latent diffusion model on these tokens for reconstruction.

3 METHODS: MODEL TRAINING AND EVALUATION

Our brain decoding model, *NeuroAdapter*, as shown in Fig. 2, is built on the IP-Adapter framework (Ye et al., 2023). We conditioned a pre-trained Stable Diffusion model¹ (SD, Rombach et al. (2022)) on fMRI-derived features via cross-attention mechanism to reconstruct perceived visual stimuli. We explain our method details for the Natural Scene Dataset (NSD, Allen et al. (2022)) but similar method applies to the other datasets as well.

3.1 NEURAL DATA PROCESSING AND PARCELLATION

We trained our model using the surface-based fMRI data in *fsaverage* space. We first averaged the vertex responses across image repetitions to obtain a single response pattern per image. To transform the high-dimensional fMRI data into structured inputs for conditioning the diffusion model, we applied the Schaefer parcellation (Schaefer et al., 2017), which clusters cortical vertices into 500 parcels per hemisphere (Appendix C).

To improve robustness of the model by restricting inputs to high-quality regions, we computed vertex-wise Signal-to-Noise Ratio (SNR) and selected top k parcels per hemisphere with the highest average SNR, yielding a total of $p = 2k$ parcels as fMRI conditioning inputs to the model. In the following sections, we report results of our model trained on $p = 200$ brain parcels, and present an ablation study on how varying p influences decoding performance in the Appendix I.

3.2 PARCEL-WISE LINEAR MAPPING

Since the number of vertices varies across parcels, we padded each parcel’s vertex response vector to match the largest vertex count across parcels v_{max} . This yields processed neural data $D_{fMRI} \in \mathbb{R}^{n \times p \times v_{max}}$. Then, each parcel was assigned a unique projection matrix $w \in \mathbb{R}^{v_{max} \times f}$, transforming padded vertex response into fMRI token embeddings $E \in \mathbb{R}^{n \times p \times f}$, where n and f are batch size and hidden dimension of fMRI token embeddings respectively. In the main text, we set $f = 768$ during model training, and results from an ablation study with different values of f is provided in the Appendix H. Additionally, we conducted another ablation study (Appendix J) to demonstrate that mapping fMRI data into the parcel-wise token space to condition the SD generation is effective for visual reconstruction.

¹<https://huggingface.co/stable-diffusion-v1-5/stable-diffusion-v1-5>

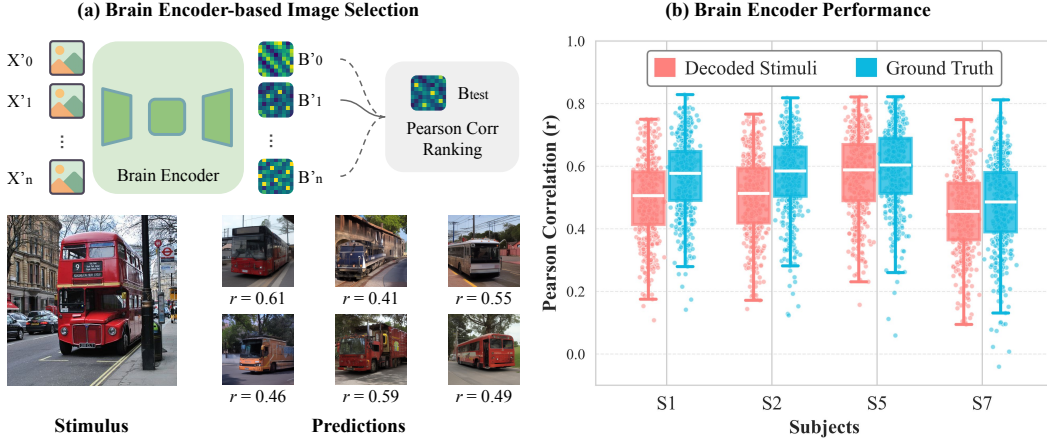


Figure 3: **Brain Encoder.** (a) Brain encoder-based image selection using Pearson correlations between predicted and measured fMRI responses for a NSD test example. (b) Red: correlation between the predicted brain activity from the decoded images and the measured brain activity. Blue: correlation between the predicted activity for the stimulus and the corresponding fMRI response.

3.3 LATENT DIFFUSION PROCESS WITH BRAIN CONDITIONING

We replaced the cross-attention layer of the U-Net (Ronneberger et al., 2015) in SD with an IP-adapter-style cross-attention module (Ye et al., 2023), enabling the model to attend to the fMRI token embeddings. To ensure that embeddings were the only conditioning input, the text encoder in SD received an empty input during both training and inference. During training, only the parcel-wise linear mapper and the new cross-attention modules were updated, with the rest of the SD parameters kept frozen.

fMRI Token Dropout. We applied a stochastic token dropout strategy during training to the fMRI token embeddings E to ensure robustness of visual decoding. We randomly dropped out parcel-wise token vectors for each training sample. A dropout probability $r \sim \mathcal{U}(0, 1)$ was drawn, and each fMRI token vector was independently retained with probability r . This resulted in a binary mask $M \in \{0, 1\}^{n \times p \times 1}$, which was applied parcel-wise to the fMRI token embeddings $E' = E \odot M$. We found this regularization to be crucial for strong decoding performance, as supported by the ablation results in Appendix G.

Min-SNR Loss Weighting. To stabilize training and improve sample quality, we adopted the min-SNR weighting strategy (Hang et al., 2023) recently introduced in diffusion models. This approach down-weights the contribution of easy high-SNR steps, where reconstructions are clean, while preserving the weight of noisy low-SNR steps, yielding a more balanced training signal across the diffusion process (please view Appendix L for details).

3.4 DECODED IMAGE SELECTION WITH BRAIN ENCODING MODEL

During evaluation, we used a brain encoder (Adeli et al., 2023; 2025) trained on the same fMRI-image training dataset to identify the best decoded stimuli. As shown in Fig. 3 (a), for each fMRI sample in the test set, we generated a set of candidate images with different random seeds. The brain encoder predicted vertex-wise fMRI activity for each candidate image, which was correlated with the measured fMRI response. The candidate image with the highest Pearson correlation was selected as the final decoded image for further evaluation. An ablation study assessing the impact of the brain encoder to decoding performance is reported in Appendix K.

4 METHODS: IBBI FRAMEWORK FOR INTERPRETABILITY

Beyond decoding performance, we also investigated the interpretability of the generative process in our model. During inference, the SD model reconstructs images by progressively denoising a latent representation over multiple steps, starting from pure Gaussian noise and gradually refining it toward a clean image. At each denoising step t , the U-Net backbone applies a sequence of downsampling and upsampling blocks, each equipped with cross-attention layers that integrate the fMRI-derived conditioning. Since the conditioning input to SD was parcel-wise embeddings, this can be represented as a token matrix $E \in \mathbb{R}^{p \times f}$ (batch size $n = 1$ for simplicity), where each row $e_i \in \mathbb{R}^f$ corresponds to the embedding of parcel P_i . If anatomical or functional labels are available for brain parcels, this formulation enables ROI-level probing of the cross-attention mechanism to see how brain representations interact with U-Net in the generative process. Following this idea, we propose the **Image-Brain BI-directional** framework (*IBBI*) for exploring the internal attention dynamics, which links brain activity and image features during decoding.

4.1 PROBLEM SETUP

In *NeuroAdapter*, each cross-attention layer computes attention scores $\text{Attn}(Q, K, V)$, where queries $Q \in \mathbb{R}^{q \times d}$ come from spatial tokens in the U-Net of SD, and keys and values $(K, V) \in \mathbb{R}^{p \times d}$ are derived from the fMRI embeddings E . At each denoising timestep t , the attention weight matrix $A^{(\ell, h, t)} \in \mathbb{R}^{q \times p}$ for head h in layer ℓ encodes the influence of each parcel token on each spatial query. Each entry of the attention weight matrix can be expressed as:

$$A_{i,j}^{(\ell, h, t)} = \frac{\exp\left(\langle Q_i^{(\ell, h, t)}, K_j^{(\ell, h, t)} \rangle / \sqrt{d}\right)}{\sum_{j'=1}^p \exp\left(\langle Q_i^{(\ell, h, t)}, K_{j'}^{(\ell, h, t)} \rangle / \sqrt{d}\right)}$$

where query index $i \in \{1, \dots, q\}$, and parcel index $j \in \{1, \dots, p\}$. Specifically, the entry $A_{i,j}^{(\ell, h, t)}$ refers to the attention from the i -th query vector $Q_i^{(\ell, h, t)}$ to the j -th parcel token, represented by its key vector $K_j^{(\ell, h, t)}$. Intuitively, each entry of this matrix reflects the degree of attention from a particular spatial query in the image to a specific parcel. Our proposed interpretability framework further exploits this matrix from two complementary views.

4.2 BRAIN-DIRECTED VIEW

We summarize the attention weight matrix $A^{(\ell, h, t)}$ over brain parcel tokens at each timestep into a vector $B^{(t)}$ (parcel contribution vector), normalized to unit mass. Formally, let L be the number of cross-attention layers in U-Net, H be the number of multi-attention heads, and q^ℓ be the number of spatial queries in layer ℓ . At the denoising step t , each cross-attention map satisfies $\sum_{j=1}^p A_{i,j}^{(\ell, h, t)} = 1$ for every (ℓ, h, i) . To aggregate the total attention mass assigned to each parcel across layers with different spatial resolutions, we weight every query equally and normalize by the total number of queries $\sum_{\ell=1}^L q^\ell$. For each parcel $j \in \{1, \dots, p\}$, we define

$$B_j^{(t)} = \frac{1}{H \sum_{\ell=1}^L q^\ell} \sum_{\ell=1}^L \sum_{h=1}^H \sum_{i=1}^{q^\ell} A_{i,j}^{(\ell, h, t)}$$

Here, $\sum_{j=1}^p B_j^{(t)} = 1$, so $B^{(t)} \in \mathbb{R}^p$ can be interpreted as a query-weighted share of attention mass over parcels at timestep t . The vector represents the *relative contribution* of different parcels.

4.3 IMAGE-DIRECTED VIEW

We are motivated by the previous work that interpreting text guidance in SD (Tang et al., 2023). In our case, the spatial structure in $A^{(\ell, h, t)}$ enables us to explore further where, in the generated image, each brain parcel or ROI (Region of Interest) directs its attention at timestep t . For a given ROI group from parcels, denoted as $\mathcal{R} \subseteq \{1, \dots, p\}$, we pool attentions across heads and ROI tokens to

form a query-wise attention profile for each layer:

$$m_{\mathcal{R}}^{(\ell,t)}(i) = \frac{1}{H} \frac{1}{|\mathcal{R}|} \sum_{h=1}^H \sum_{j \in \mathcal{R}} A_{i,j}^{(\ell,h,t)}$$

The vector $m_{\mathcal{R}}^{(\ell,t)} \in \mathbb{R}^{q^\ell}$ is then reshaped to a 2D map, which matches the spatial grid of the layer ℓ . Because the spatial resolution varies across downsampling and upsampling blocks of the U-Net, we upsample each 2D map to full image resolution, yielding $U_{\mathcal{R}}^{(\ell,t)} \in \mathbb{R}^{H_{\text{img}} \times W_{\text{img}}}$ for every cross-attention layer. To produce overlays that are comparable for spatial location across ROIs, we normalize each upsampled map to unit L_1 mass and then average uniformly across layers:

$$I_{\mathcal{R}}^{(t)} = \frac{1}{L} \sum_{\ell=1}^L \frac{U_{\mathcal{R}}^{(\ell,t)}}{\sum_{x,y} U_{\mathcal{R}}^{(\ell,t)}(x,y)}$$

We refer to $I_{\mathcal{R}}^{(t)}$ as the ROI attention maps, which highlights *where* a given ROI allocates its attention in the image at timestep t . Intuitively, ROI attention maps provide a functional footprint of each ROI in the stimulus space, allowing us to interpret the role of neural data from different parts of the brain in shaping specific image regions during reconstruction.

5 EXPERIMENTS

5.1 DATASETS

Natural Scene Dataset (NSD). We used the NSD, a large-scale 7T-fMRI dataset designed for studying visual representations in the human brain (Allen et al., 2022). This contains high-resolution brain responses from 8 subjects, each viewing up to 10,000 distinct natural images sampled from the MSCOCO dataset (Lin et al., 2014). In our experiments, we trained our brain decoding model and brain encoding model (mentioned in Section 3.4) on the NSD data following the standard preprocessing steps. In the following sections, we report comparisons with prior work using the averaged results from 4 subjects who completed entire fMRI scanning sessions (subjects 1, 2, 5, 7). For the relevant ablation studies, we restrict our analysis to subject 1 and evaluate models under different experimental conditions on this single-subject dataset.

NSD-Imagery. We further evaluated our framework on the NSD-Imagery dataset (Kneeland et al., 2025), an extension of the NSD designed to study brain activity during mental imagery. NSD-Imagery contains high-resolution 7T-fMRI recordings from the same 8 participants as NSD, with trials including simple geometric patterns, complex natural scenes, and conceptual word cues. During imagery runs, subjects were cued with a letter and instructed to vividly imagine the corresponding stimulus without physically seeing it. Each subject completed 12 runs (9 run types with imagery runs repeated twice), yielding 576 trials per participant. In our experiments, we directly evaluated our models, which are trained on NSD, on this dataset to see if our model can generalize to mental imagery tasks.

Deeprecon Dataset (Deeprecon). The Deeprecon dataset (Shen et al., 2019b) comprises fMRI activity data from 5 subjects who viewed both ImageNet images and artificial images. The dataset contains 1,200 distinct natural images for training (each presented with 5 repetitions), 50 natural images and 40 artificial images for testing (each presented over 20 repetitions), totaling 8,000 brain samples per subject. An important consideration for this dataset was that natural test images were selected from ImageNet categories that differed from the training categories, and artificial images were included as additional test stimuli. For this dataset, we trained our brain decoder and encoder on 16 brain parcels across the two hemispheres, including early visual areas (V1, V2, V3), V4, higher-order visual regions (LOC, FFA, PPA), and the broader higher visual cortex (HVC) region.

5.2 EVALUATION METRICS

We evaluated the model’s performance using the following 8 image quality metrics that are commonly used in the literature. *PixCorr* measures the pixel-level correlation between reconstructed

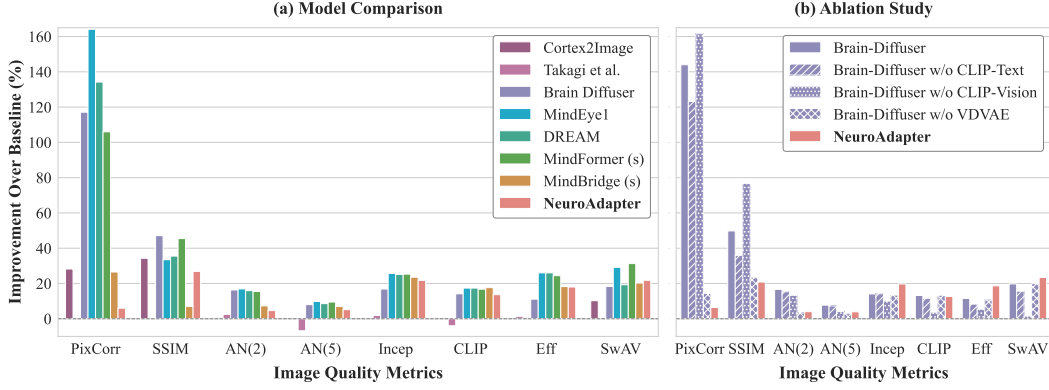


Figure 5: **Model Comparison.** Decoding performance across eight image quality metrics, comparing prior approaches and our method. To ensure fair comparison, results are shown as relative improvements over a subject-specific ImageNet-retrieval baseline. (a) *NeuroAdapter* achieves competitive performance with embedding-aligned approaches, particularly on high-level semantic metrics. (b) Comparison with *Brain Diffuser* variants shows that their advantage on low-level metrics arises from a dedicated pathway for predicting latent visual features (VDVAE), whereas removing this pathway yields performance on low-level metrics comparable to ours.

matching based decoding approaches inspired by Kay et al. (2008). Examples of the baseline are shown in Appendix B.

From Fig. 5 (a), we observe that *NeuroAdapter* achieves competitive performance with, and in some cases surpasses, embedding-aligned approaches on high-level semantic metrics. This pattern suggests that our model, despite its simplicity, is particularly effective at capturing semantic content encoded in the fMRI signals without the use of an intermediate image representation (Fig. 4, Appendix A).

At the same time, our approach also captures low-level metrics reasonably well compared to the baseline retrieval method, although these improvements are more modest compared to those reported by other methods. To better understand the reason behind this, we compared our performance with *Brain Diffuser* models using different embedding spaces. As evident in Fig. 5 (b), the better performance comes from the separate pathway that those models have for predicting low-level latent features and removing them as in the case of *Brain-Diffuser w/o VDVAE* makes their performance comparable to ours on low level metrics. By design, we chose not to include such a pathway in *NeuroAdapter* and instead have a more direct and interpretable link between brain activity and image reconstruction (see Section 6.2).

We further compare the correlation between the predicted brain activity from the decoded images and the original ground truth activity (Fig. 3 (b) in red). We also show the correlation between the predicted activity for the ground truth image and the corresponding measured fMRI response (Fig. 3 (b) in blue). This figure shows that the decoded images have visual properties that leads to fMRI activity that is very similar to the original image, further strengthening our decoding results.

We report performance of our model on two additional datasets, NSD-Imagery and Deeprecon, (Kneeland et al., 2025; Shen et al., 2019b) with quantitative and qualitative results reported in the Appendix F, E, O, and P. On NSD-Imagery, *NeuroAdapter* demonstrates comparable generalization ability across both mental imagery and vision trials compared to existing work, especially for high-level semantic metrics. Experiments on Deeprecon, where training and test classes are disjoint, suggest that *NeuroAdapter* is able to infer not only category-level information but also finer low-level visual properties such as shape (e.g., coin), orientation (e.g., instrument), and color (e.g., reddish reconstructions for pink artificial shapes). To our knowledge, no existing modern decoding models have been quantitatively evaluated on Deeprecon, and we provide our results as a baseline for future research.

6.2 INTERPRETABILITY

In this section, we visualize and analyze how brain representations influence the generative process with cross attention in *NeuroAdapter*. As mentioned in Section 4, our proposed *IBBI* framework provides two complementary perspectives, showing how different brain regions contribute to visual reconstruction and where those ROIs direct their attention in the pixel-level stimulus space.

Brain-directed View. Based on the parcel contribution vector, we averaged $B^{(t)}$ across timesteps to obtain a global view $\bar{B}^{(t)}$ summarizing parcel contributions throughout the generative process. The 200 parcels and their corresponding contribution weights were projected onto the cortical surface for visualization. For easy interpretation through the visualization (Fig. 6), we ranked the parcels by their average contribution and divided them into five partitions (top 20%, 20–40%, 40–60%, 60–80%, and bottom 20%). This partitioning highlights the relative importance of different cortical regions, enabling us to identify high-impact parcels that dominate the generative trajectory and low-impact parcels that play only minor roles.

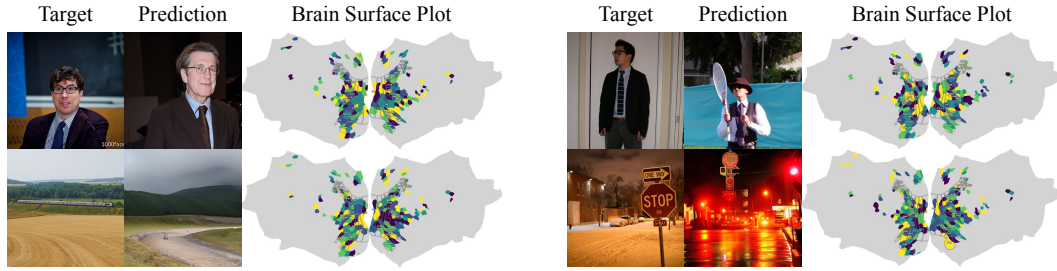


Figure 6: **Example projections of parcel contribution vector onto the cortical surface.**

Image-directed View. Here, we visualize the ROI attention maps (RAM) across generative timesteps for representative category-selective regions, including *Face*, *Body*, *Scene*, and *Word*. Fig. 7 reveals how different cortical ROIs guide attention toward distinct spatial locations in the image during the unfolding denoising process, thereby linking regional neural signals to specific pixel-level features. Additional examples of ROI attention maps are provided in Appendix M.

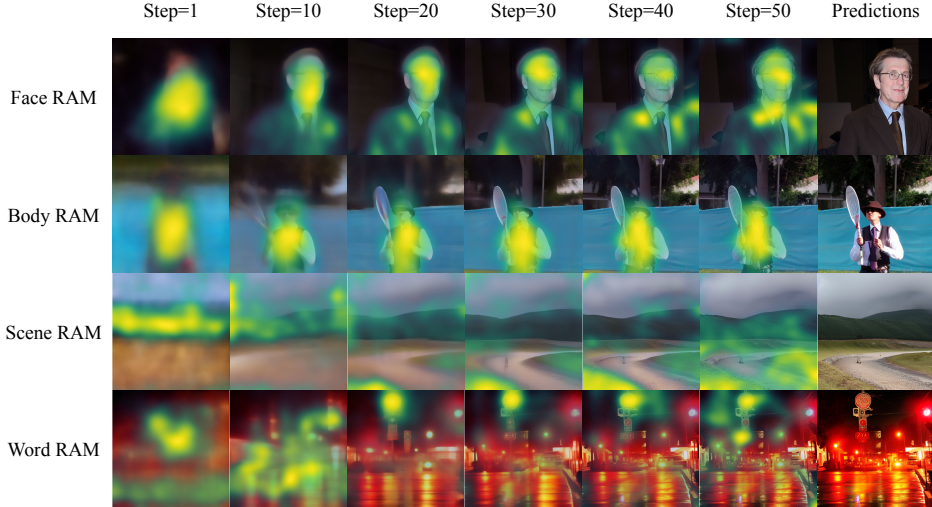


Figure 7: **ROI attention map dynamics across generative timesteps.**

Causal Perturbation Analysis. Having the parcel-wise linear mapping further allows us to perform perturbation analysis, in which we mask specific ROIs and examine how this manipulation alters the reconstructed images. Consistent with the selectivity of different ROIs, we observe that

masking low-level ROIs does not compromise the semantic content of the generated images, but masking high-level ROIs completely changes them (See Appendix N for ablation details).

7 DISCUSSION

We present an effective end-to-end brain-decoding framework that directly conditions the diffusion denoising process on brain activity, bypassing intermediate feature spaces and enabling both effective decoding and mechanistic interpretability. Our results show that this approach achieves competitive reconstruction quality, particularly on high-level semantic metrics. Due to the stochastic nature of the diffusion model, we see a great variability in the quality of the generated images. While our encoder based selection addresses this limitation to some extent, future work will have to better understand the mapping from brain activity to images and make model performance more consistent. We believe this will be a great use case for the developed interpretability methods in this domain.

Meanwhile, we notice that current brain-decoding benchmarks may be approaching saturation when evaluated solely through image quality metrics. Improvements in these scores do not necessarily reflect faithful brain decoding, as they may also result from stronger alignment with pretrained embedding spaces or simply the use of more powerful generative models. Therefore, our *IBBI* framework provides a complementary perspective, aiming to reveal how cortical parcels contribute to and shape the unfolding generative process, thereby linking brain activity and image features in a bi-directional manner. Looking ahead, future progress in brain decoding will depend on both methodological advances and richer interpretability frameworks, moving beyond metric-driven evaluation toward a deeper understanding of the neural–generative interface.

REPRODUCIBILITY STATEMENT

We have made every effort to ensure the reproducibility of our work. Details of the datasets used, including NSD core, NSD imagery and Deeprecon, are provided in Section 5.1. The architecture of *NeuroAdapter*, training objectives and evaluation setup are described in Section 3. Our interpretability framework (*IBBI*) is fully specified in Section 4, including the mathematical definitions. We also provide results of ablation studies in appendices to verify the robustness of our results. For computational reproducibility, our models were trained on a university GPU cluster with 2 NVIDIA L40 GPUs. Each model was trained for 300 epochs with a batch size of 16, requiring approximately 25 hours of training time. Source code, along with instructions for reproducing all experiments will be released once the paper gets accepted.

THE USE OF LARGE LANGUAGE MODELS (LLMs)

Large Language Models (LLMs) were used in this project as general-purpose assistant tools. Specifically, we used GitHub Copilot with Claude 3.7 to help sort and refactor code for readability and debugging during the research process, and used OpenAI ChatGPT-5 to polish the writing for clarity and effective communication of our ideas. No part of the model design, experimental results, or scientific conclusions depended on LLMs.

REFERENCES

- Hossein Adeli, Sun Minni, and Nikolaus Kriegeskorte. Predicting brain activity using transformers. *bioRxiv*, pp. 2023–08, 2023.
- Hossein Adeli, Minni Sun, and Nikolaus Kriegeskorte. Transformer brain encoders explain human high-level visual responses. *arXiv preprint arXiv:2505.17329*, 2025.
- E. J. Allen et al. A massive 7T fMRI dataset to bridge cognitive neuroscience and artificial intelligence. *Nature Neuroscience*, 25:116–126, 2022. doi: 10.1038/s41593-021-00962-x.
- Mathilde Caron, Ishan Misra, Julien Mairal, Priya Goyal, Piotr Bojanowski, and Armand Joulin. Unsupervised learning of visual features by contrasting cluster assignments. In *Proceedings of*

- the 34th International Conference on Neural Information Processing Systems, NIPS '20, Red Hook, NY, USA, 2020. Curran Associates Inc. ISBN 9781713829546.
- Mathilde Caron, Hugo Touvron, Ishan Misra, Herv'e J'egou, Julien Mairal, Piotr Bojanowski, and Armand Joulin. Emerging properties in self-supervised vision transformers. *2021 IEEE/CVF International Conference on Computer Vision (ICCV)*, pp. 9630–9640, 2021. URL <https://api.semanticscholar.org/CorpusID:233444273>.
- Zijiao Chen, Jiabin Qing, Tiange Xiang, Wan Lin Yue, and Juan Helen Zhou. Seeing beyond the brain: Conditional diffusion model with sparse masked modeling for vision decoding. In *Proceedings of the IEEE/CVF Conference on Computer Vision and Pattern Recognition*, pp. 22710–22720, 2023.
- Fan L Cheng, Tomoyasu Horikawa, Kei Majima, Misato Tanaka, Mohamed Abdelhack, Shuntaro C Aoki, Jin Hirano, and Yukiyasu Kamitani. Reconstructing visual illusory experiences from human brain activity. *Science Advances*, 9(46):eadj3906, 2023.
- Jia Deng, Wei Dong, Richard Socher, Li-Jia Li, Kai Li, and Li Fei-Fei. Imagenet: A large-scale hierarchical image database. In *2009 IEEE conference on computer vision and pattern recognition*, pp. 248–255. Ieee, 2009.
- James S. Gao, Alexander G. Huth, Mark D. Lescroart, and Jack L. Gallant. Pycortex: an interactive surface visualizer for fMRI. *Frontiers in Neuroinformatics*, 9, September 2015. ISSN 1662-5196. doi: 10.3389/fninf.2015.00023. URL <http://journal.frontiersin.org/Article/10.3389/fninf.2015.00023/abstract>.
- Zixuan Gong, Qi Zhang, Guanyin Bao, Lei Zhu, Rongtao Xu, Ke Liu, Liang Hu, and Duoqian Miao. Mindtuner: Cross-subject visual decoding with visual fingerprint and semantic correction. In *Proceedings of the AAAI Conference on Artificial Intelligence*, volume 39, pp. 14247–14255, 2025.
- Zijin Gu, Keith Jamison, Amy Kuceyeski, and Mert R. Sabuncu. Decoding natural image stimuli from fmri data with a surface-based convolutional network. In Ipek Oguz, Jack Noble, Xiaoxiao Li, Martin Styner, Christian Baumgartner, Mirabela Rusu, Tobias Heinmann, Despina Kontos, Bennett Landman, and Benoit Dawant (eds.), *Medical Imaging with Deep Learning*, volume 227 of *Proceedings of Machine Learning Research*, pp. 107–118. PMLR, 10–12 Jul 2024. URL <https://proceedings.mlr.press/v227/gu24a.html>.
- Inhwa Han, Jaayeon Lee, and Jong Chul Ye. Mindformer: Semantic alignment of multi-subject fmri for brain decoding. *arXiv preprint arXiv:2405.17720*, 2024.
- Tiankai Hang, Shuyang Gu, Chen Li, Jianmin Bao, Dong Chen, Han Hu, Xin Geng, and Baining Guo. Efficient diffusion training via min-snr weighting strategy. In *Proceedings of the IEEE/CVF International Conference on Computer Vision (ICCV)*, pp. 7441–7451, October 2023.
- Jingyang Huo, Yikai Wang, Yun Wang, Xuelin Qian, Chong Li, Yanwei Fu, and Jianfeng Feng. Neuropictor: Refining fmri-to-image reconstruction via multi-individual pretraining and multi-level modulation. In *European Conference on Computer Vision*, pp. 56–73. Springer, 2024.
- Kendrick N. Kay, Thomas Naselaris, Ryan J. Prenger, and Jack L. Gallant. Identifying natural images from human brain activity. *Nature*, 452(7185):352–355, March 2008. ISSN 0028-0836. doi: 10.1038/nature06713.
- Reese Kneeland, Paul S. Scotti, Ghislain St-Yves, Jesse Breedlove, Kendrick Kay, and Thomas Naselaris. Nsd-imagery: A benchmark dataset for extending fmri vision decoding methods to mental imagery. In *2025 IEEE/CVF Conference on Computer Vision and Pattern Recognition (CVPR)*, pp. 28852–28862. IEEE, June 2025. doi: 10.1109/cvpr52734.2025.02687. URL <http://dx.doi.org/10.1109/CVPR52734.2025.02687>.
- Alex Krizhevsky, Ilya Sutskever, and Geoffrey E. Hinton. Imagenet classification with deep convolutional neural networks. In *Proceedings of the 26th International Conference on Neural Information Processing Systems - Volume 1, NIPS'12*, pp. 1097–1105, Red Hook, NY, USA, 2012. Curran Associates Inc.

- Haoyu Li et al. Neuraldiffuser: Neuroscience-inspired diffusion guidance for fmri visual reconstruction. *IEEE Transactions on Image Processing*, 34:552–565, 2025. ISSN 1941-0042. doi: 10.1109/tip.2025.3526051.
- Sikun Lin, Thomas Sprague, and Ambuj K Singh. Mind reader: reconstructing complex images from brain activities. In *Proceedings of the 36th International Conference on Neural Information Processing Systems*, NIPS ’22, Red Hook, NY, USA, 2022. Curran Associates Inc. ISBN 9781713871088.
- Tsung-Yi Lin, Michael Maire, Serge Belongie, James Hays, Pietro Perona, Deva Ramanan, Piotr Dollár, and C. Lawrence Zitnick. *Microsoft COCO: Common Objects in Context*, pp. 740–755. Springer International Publishing, 2014. ISBN 9783319106021. doi: 10.1007/978-3-319-10602-1_48. URL http://dx.doi.org/10.1007/978-3-319-10602-1_48.
- David Mayo, Christopher Wang, Asa Harbin, Abdulrahman Alabdulkareem, Albert Eaton Shaw, Boris Katz, and Andrei Barbu. Brainbits: How much of the brain are generative reconstruction methods using? In *The Thirty-eighth Annual Conference on Neural Information Processing Systems*, 2024. URL <https://openreview.net/forum?id=KAAUvi4kpb>.
- Maxime Oquab, Timothée Darcet, Theo Moutakanni, Huy V. Vo, Marc Szafraniec, Vasil Khalidov, Pierre Fernandez, Daniel Haziza, Francisco Massa, Alaaeldin El-Nouby, Russell Howes, Po-Yao Huang, Hu Xu, Vasu Sharma, Shang-Wen Li, Wojciech Galuba, Mike Rabbat, Mido Assran, Nicolas Ballas, Gabriel Synnaeve, Ishan Misra, Herve Jegou, Julien Mairal, Patrick Labatut, Armand Joulin, and Piotr Bojanowski. Dinov2: Learning robust visual features without supervision, 2023.
- Furkan Ozelik and Rufin VanRullen. Natural scene reconstruction from fmri signals using generative latent diffusion, 2023. URL <https://arxiv.org/abs/2303.05334>.
- Alec Radford, Jong Wook Kim, Chris Hallacy, Aditya Ramesh, Gabriel Goh, Sandhini Agarwal, Girish Sastry, Amanda Askell, Pamela Mishkin, Jack Clark, et al. Learning transferable visual models from natural language supervision. In *International conference on machine learning*, pp. 8748–8763. PmLR, 2021.
- Robin Rombach, Andreas Blattmann, Dominik Lorenz, Patrick Esser, and Björn Ommer. High-resolution image synthesis with latent diffusion models. In *Proceedings of the IEEE/CVF Conference on Computer Vision and Pattern Recognition (CVPR)*, pp. 10684–10695, June 2022.
- Olaf Ronneberger, Philipp Fischer, and Thomas Brox. *U-Net: Convolutional Networks for Biomedical Image Segmentation*, pp. 234–241. Springer International Publishing, 2015. ISBN 9783319245744. doi: 10.1007/978-3-319-24574-4_28. URL http://dx.doi.org/10.1007/978-3-319-24574-4_28.
- Alexander Schaefer, Ru Kong, Evan M Gordon, Timothy O Laumann, Xi-Nian Zuo, Avram J Holmes, Simon B Eickhoff, and B T Thomas Yeo. Local-global parcellation of the human cerebral cortex from intrinsic functional connectivity mri. *Cerebral Cortex*, 28(9):3095–3114, July 2017. ISSN 1460-2199. doi: 10.1093/cercor/bhx179.
- Paul Scotti, Atmadeep Banerjee, Jimmie Goode, Stepan Shabalin, Alex Nguyen, Aidan Dempster, Nathalie Verlinde, Elad Yundler, David Weisberg, Kenneth Norman, et al. Reconstructing the mind’s eye: fmri-to-image with contrastive learning and diffusion priors. *Advances in Neural Information Processing Systems*, 36:24705–24728, 2023.
- Paul S. Scotti, Mihir Tripathy, Cesare Kadir Torricco Villanueva, Reese Kneeland, Tong Chen, Ashutosh Narang, Charan Santhirasegaran, Jonathan Xu, Thomas Naselaris, Kenneth A. Norman, and Tanishq Mathew Abraham. Mindeye2: shared-subject models enable fmri-to-image with 1 hour of data. In *Proceedings of the 41st International Conference on Machine Learning, ICML’24*. JMLR.org, 2024.
- Katja Seeliger, Umut Güçlü, Luca Ambrogioni, Yagmur Güçlütürk, and Marcel AJ Van Gerven. Generative adversarial networks for reconstructing natural images from brain activity. *NeuroImage*, 181:775–785, 2018.

- Guohua Shen, Kshitij Dwivedi, Kei Majima, Tomoyasu Horikawa, and Yukiyasu Kamitani. End-to-end deep image reconstruction from human brain activity. *Frontiers in computational neuroscience*, 13:21, 2019a.
- Guohua Shen, Tomoyasu Horikawa, Kei Majima, and Yukiyasu Kamitani. Deep image reconstruction from human brain activity. *PLoS computational biology*, 15(1):e1006633, 2019b.
- Oriane Siméoni, Huy V. Vo, Maximilian Seitzer, Federico Baldassarre, Maxime Oquab, Cijo Jose, Vasil Khalidov, Marc Szafraniec, Seungeun Yi, Michaël Ramamonjisoa, Francisco Massa, Daniel Haziza, Luca Wehrstedt, Jianyuan Wang, Timothée Darcet, Théo Moutakanni, Leonel Sentana, Claire Roberts, Andrea Vedaldi, Jamie Tolan, John Brandt, Camille Couprie, Julien Mairal, Hervé Jégou, Patrick Labatut, and Piotr Bojanowski. DINOv3, 2025. URL <https://arxiv.org/abs/2508.10104>.
- Christian Szegedy, Vincent Vanhoucke, Sergey Ioffe, Jon Shlens, and Zbigniew Wojna. Rethinking the inception architecture for computer vision. In *Proceedings of the IEEE conference on computer vision and pattern recognition*, pp. 2818–2826, 2016.
- Yu Takagi and Shinji Nishimoto. High-resolution image reconstruction with latent diffusion models from human brain activity. In *Proceedings of the IEEE/CVF Conference on Computer Vision and Pattern Recognition (CVPR)*, pp. 14453–14463, June 2023.
- Mingxing Tan and Quoc Le. EfficientNet: Rethinking model scaling for convolutional neural networks. In Kamalika Chaudhuri and Ruslan Salakhutdinov (eds.), *Proceedings of the 36th International Conference on Machine Learning*, volume 97 of *Proceedings of Machine Learning Research*, pp. 6105–6114. PMLR, 09–15 Jun 2019. URL <https://proceedings.mlr.press/v97/tan19a.html>.
- Raphael Tang, Linqing Liu, Akshat Pandey, Zhiying Jiang, Gefei Yang, Karun Kumar, Pontus Stenetorp, Jimmy Lin, and Ferhan Ture. What the DAAM: Interpreting stable diffusion using cross attention. In Anna Rogers, Jordan Boyd-Graber, and Naoaki Okazaki (eds.), *Proceedings of the 61st Annual Meeting of the Association for Computational Linguistics (Volume 1: Long Papers)*, pp. 5644–5659, Toronto, Canada, July 2023. Association for Computational Linguistics. doi: 10.18653/v1/2023.acl-long.310. URL <https://aclanthology.org/2023.acl-long.310/>.
- Shizun Wang, Songhua Liu, Zhenxiong Tan, and Xinchao Wang. Mindbridge: A cross-subject brain decoding framework. In *Proceedings of the IEEE/CVF Conference on Computer Vision and Pattern Recognition*, pp. 11333–11342, 2024.
- Zhou Wang, A.C. Bovik, H.R. Sheikh, and E.P. Simoncelli. Image quality assessment: from error visibility to structural similarity. *IEEE Transactions on Image Processing*, 13(4):600–612, 2004. doi: 10.1109/TIP.2003.819861.
- Weihaio Xia, Raoul De Charette, Cengiz Oztireli, and Jing-Hao Xue. Dream: Visual decoding from reversing human visual system. In *Proceedings of the IEEE/CVF Winter Conference on Applications of Computer Vision*, pp. 8226–8235, 2024.
- Hu Ye, Jun Zhang, Sibio Liu, Xiao Han, and Wei Yang. Ip-adapter: Text compatible image prompt adapter for text-to-image diffusion models. 2023.
- Bohan Zeng, Shanglin Li, Xuhui Liu, Sicheng Gao, Xiaolong Jiang, Xu Tang, Yao Hu, Jianzhuang Liu, and Baochang Zhang. Controllable mind visual diffusion model. In *Proceedings of the AAAI conference on artificial intelligence*, volume 38, pp. 6935–6943, 2024.

APPENDIX

A EXAMPLES OF DECODED STIMULI ON NSD

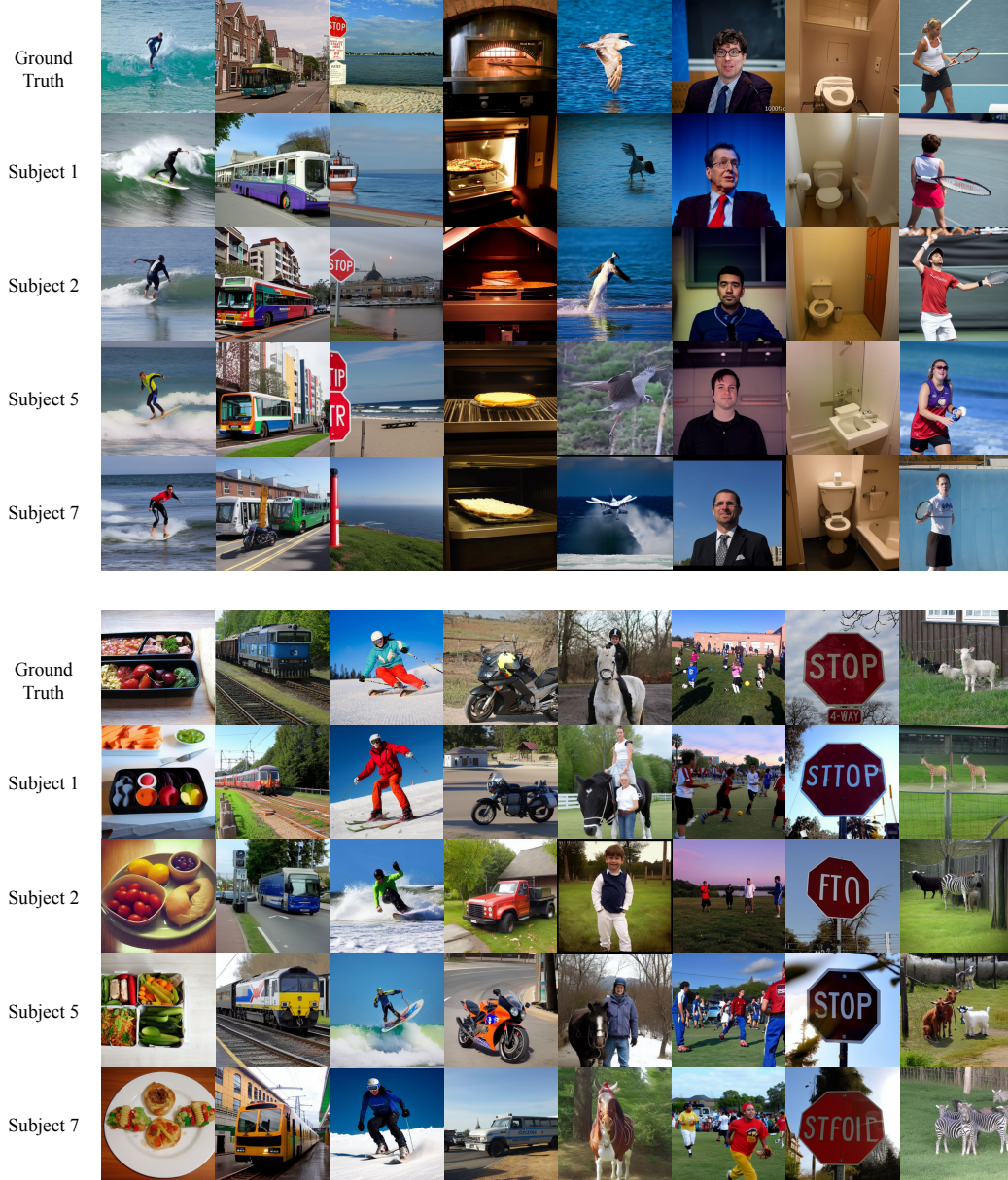


Figure 8: Examples of ground truth with corresponding decoded stimuli across subjects

B EXAMPLES OF IMAGENET RETRIEVAL BASELINES

We present shared retrieved images across 4 subjects in this figure. In our experiment, we created and evaluated baselines separately for each subject.

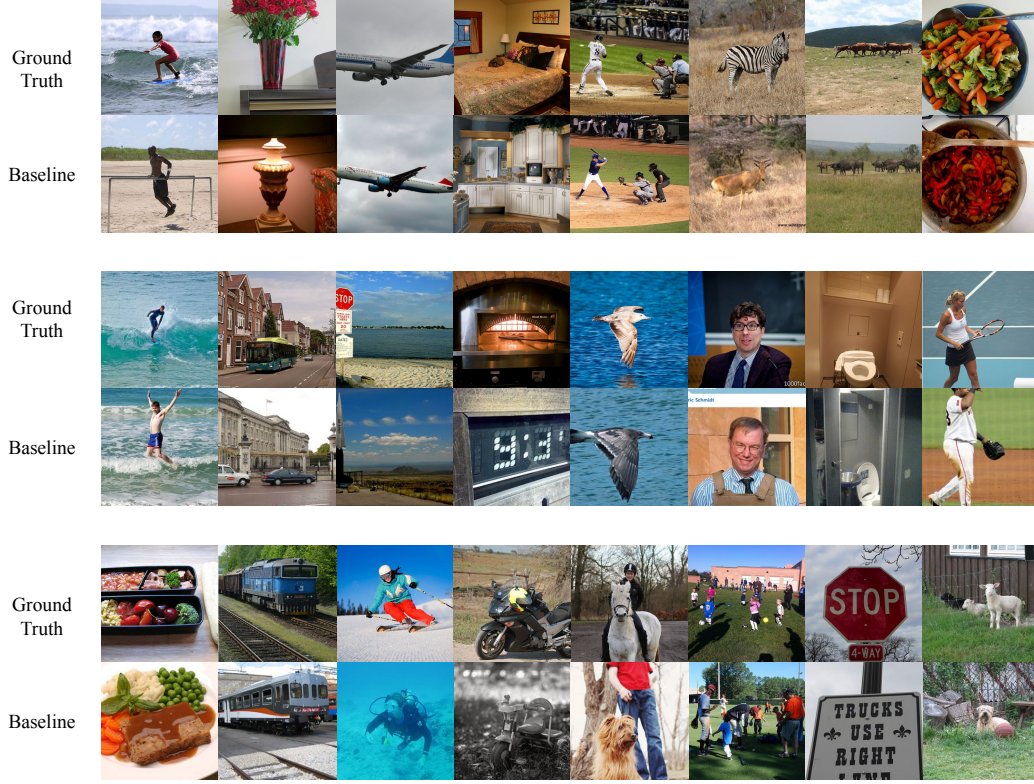


Figure 9: Ground Truth vs. ImageNet Retrieval Baselines.

C SCHAEFER PARCELLATION

To represent brain activity at the regional level, we adopt the Schaefer cortical parcellation (Fig. 10). This provides a functional subdivision of the cortex derived from large-scale resting-state fMRI. In our experiments, we compute vertex-wise Signal-to-Noise Ratio (SNR) and select top 100 parcels per hemisphere with the highest average SNR.

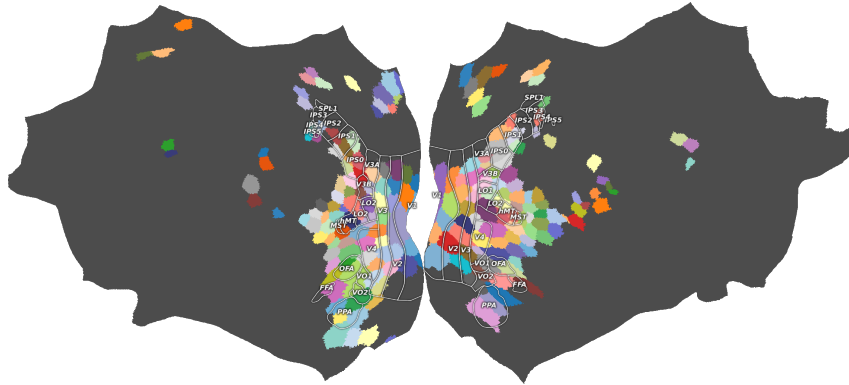


Figure 10: Top-100-SNR Parcels for each brain hemisphere displayed on the cortical surface.

D MODEL PERFORMANCE ON NSD

Table 1: Performance across different image quality metrics

Method	Low-Level				High-Level			
	PixCorr \uparrow	SSIM \uparrow	Alex(2) \uparrow	Alex(5) \uparrow	Incep \uparrow	CLIP \uparrow	Eff \downarrow	SwAV \downarrow
Baseline	.117	.242	80.98%	89.05%	74.62%	80.16%	.872	.518
Cortex2Image	.150	.325	–	–	–	–	.862	.465
Takagi et al.	–	–	83.0%	83.0%	76.0%	77.0%	–	–
Brain Diffuser	.254	.356	94.2%	96.2%	87.2%	91.5%	.775	.423
MindEye1	.309	.323	94.7%	97.8%	93.8%	94.1%	.645	.367
DREAM	.274	.328	93.9%	96.7%	93.4%	94.1%	.645	.418
MindFormer (s)	.241	.352	93.5%	97.5%	93.5%	93.6%	.659	.356
MindBridge (s)	.148	.259	86.9%	95.3%	92.2%	94.3%	.713	.413
NeuroAdapter	.124	.307	84.54%	93.48%	90.79%	90.97%	.716	.408

Table 2: NeuroAdapter vs. Brain-Diffuser performance on data from Subject 1

Method	Low-Level				High-Level			
	PixCorr \uparrow	SSIM \uparrow	Alex(2) \uparrow	Alex(5) \uparrow	Incep \uparrow	CLIP \uparrow	Eff \downarrow	SwAV \downarrow
Baseline	.125	.245	82.88%	90.41%	76.98%	81.72%	.868	.517
BD	.305	.367	96.7%	97.4%	87.8%	92.5%	.768	.415
BD w/o CLIP-Text	.279	.333	95.6%	97.0%	87.9%	91.2%	.796	.436
BD w/o CLIP-Vision	.327	.433	93.9%	94.1%	84.7%	84.5%	.821	.509
BD w/o VDVAE	.143	.302	85.6%	93.0%	87.3%	92.6%	.775	.414
NeuroAdapter	.133	.296	86.22%	93.96%	92.15%	92.03%	.706	.396

E MODEL PERFORMANCE ON NSD-IMAGERY

Table 3: NSD-Imagery: Mental Imagery vs. Vision Trials

Method	Low-Level				High-Level			
	PixCorr \uparrow	SSIM \uparrow	Alex(2) \uparrow	Alex(5) \uparrow	Incep \uparrow	CLIP \uparrow	Eff \downarrow	SwAV \downarrow
NSD-Imagery Mental Imagery Trials								
MindEye1	<u>.086</u>	.349	59.56%	61.00%	52.03%	<u>54.72%</u>	<u>.948</u>	<u>.564</u>
Brain Diffuser	.064	.401	52.14%	58.35%	<u>52.73%</u>	54.07%	.935	.585
iCNN	.108	.340	50.57%	55.25%	49.39%	41.72%	.994	.560
MindEye2	.036	<u>.414</u>	47.60%	55.38%	46.02%	50.78%	.966	.591
Takagi et al.	-.006	.455	41.88%	40.19%	43.26%	40.08%	.976	.606
NeuroAdapter	.037	.312	<u>58.90%</u>	<u>58.71%</u>	57.26%	60.04%	.970	.603
NSD-Imagery Vision Trials								
MindEye1	<u>.218</u>	.412	<u>73.56%</u>	<u>80.81%</u>	62.44%	65.34%	.881	.510
Brain Diffuser	.107	<u>.455</u>	60.34%	72.84%	60.95%	58.31%	.908	.555
iCNN	.224	.385	71.67%	81.35%	61.16%	49.03%	.926	.524
MindEye2	.161	.480	70.10%	77.52%	<u>62.69%</u>	<u>65.93%</u>	<u>.886</u>	<u>.512</u>
Takagi et al.	-.013	.412	41.55%	39.26%	39.26%	43.01%	.969	.610
NeuroAdapter	.077	.342	75.76%	78.54%	68.18	70.45%	.945	.576

F MODEL PERFORMANCE ON DEEPPRECON

Table 4: Performance on Deeprecon natural images

Condition: Token dropout, num of preds	Low-Level				High-Level			
	PixCorr ↑	SSIM ↑	Alex(2) ↑	Alex(5) ↑	Incep ↑	CLIP ↑	Eff ↓	SwAV ↓
wo/ keep low-level, 4	.087	.309	77.7%	86.6%	74.2%	81.0%	.902	.552
wo/ keep low-level, 8	.093	.310	79.1%	87.6%	74.8%	81.3%	.898	.545
wo/ keep low-level, 16	.102	.314	80.0%	88.8%	74.6%	81.7%	.892	.546
keep low-level, 4	.088	.316	78.8%	86.9%	73.4%	80.8%	.908	.552
keep low-level, 8	.084	.314	79.5%	87.0%	72.6%	81.1%	.907	.550
keep low-level, 16	.081	.311	79.9%	87.0%	71.2%	80.0%	.908	.553

Table 5: Performance on Deeprecon artificial shapes

Conditions Token dropout, num of preds	Low-Level				High-Level			
	PixCorr ↑	SSIM ↑	Alex(2) ↑	Alex(5) ↑	Incep ↑	CLIP ↑	Eff ↓	SwAV ↓
wo/ keep low-level, 4	.050	.484	63.0%	55.7%	51.2%	52.1%	.960	.622
wo/ keep low-level, 8	.062	.485	63.2%	56.4%	53.2%	50.6%	.958	.622
wo/ keep low-level, 16	.067	.477	57.1%	53.4%	53.1%	52.4%	.961	.626
keep low-level, 4	.057	.470	59.7%	55.0%	51.3%	52.3%	.958	.622
keep low-level, 8	.056	.475	62.6%	54.7%	51.2%	52.8%	.958	.621
keep low-level, 16	.057	.478	61.8%	55.8%	52.9%	51.8%	.955	.622

G ABLATION STUDY: BRAIN TOKEN DROPOUT

We conducted an ablation study to evaluate the effect of the proposed fMRI token dropout (TD) strategy in training on decoding performance. As shown in Table 6, removing token dropout substantially compromised performance across almost all metrics.

Table 6: Effect of parcel-wise token dropout (TD) on model performance

Conditions	Low-Level				High-Level			
	PixCorr ↑	SSIM ↑	Alex(2) ↑	Alex(5) ↑	Incep ↑	CLIP ↑	Eff ↓	SwAV ↓
without TD	.038	.307	67.4%	75.5%	61.2%	64.8%	.974	.666
with TD	.133	.296	86.22%	93.96%	92.15%	92.03%	.706	.396

H ABLATION STUDY: NUMBER OF CONDITION DIMENSION

Table 7: Effect of different condition dimension (CD) on model performance

Conditions	Low-Level				High-Level			
	PixCorr ↑	SSIM ↑	Alex(2) ↑	Alex(5) ↑	Incep ↑	CLIP ↑	Eff ↓	SwAV ↓
CD = 1024	.116	.303	81.49%	91.64%	88.17%	90.33%	.742	.432
CD = 960	.134	.302	85.49%	93.38%	91.32%	90.62%	.720	.410
CD = 768	.133	.296	86.22%	93.96%	92.15%	92.03%	.706	.396
CD = 576	.132	.297	86.31%	93.87%	90.42%	90.76%	.712	.400
CD = 384	.136	.301	85.65%	94.16%	89.78%	90.13%	.725	.411
CD = 192	.122	.290	85.25%	94.17%	91.33%	90.78%	.718	.417

I ABLATION STUDY: NUMBER OF HIGHEST-SNR PARCELS

Table 8: Effect of number of highest-SNR parcels (p) on model performance

Conditions	Low-Level				High-Level			
	PixCorr \uparrow	SSIM \uparrow	Alex(2) \uparrow	Alex(5) \uparrow	Incep \uparrow	CLIP \uparrow	Eff \downarrow	SwAV \downarrow
$p = 100$.106	.296	84.87%	93.65%	88.52%	90.41%	.730	.414
$p = 200$.133	.296	86.22%	93.96%	92.15%	92.03%	.706	.396
$p = 500$.094	.307	77.83%	88.93%	85.84%	88.66%	.767	.449
$p = 1000$.086	.297	76.37%	88.09%	83.95%	84.89%	.778	.457

J ABLATION STUDY: PARCEL-WISE LINEAR MAPPER

Table 9: Effect of parcel-wise linear mapper (LM) on model performance

Conditions	Low-Level				High-Level			
	PixCorr \uparrow	SSIM \uparrow	Alex(2) \uparrow	Alex(5) \uparrow	Incep \uparrow	CLIP \uparrow	Eff \downarrow	SwAV \downarrow
with LM	.133	.296	86.22%	93.96%	92.15%	92.03%	.706	.396
w/o LM	.073	.318	73.81%	82.47%	76.20%	78.11%	.843	.515

K ABLATION STUDY: BRAIN ENCODER AS A RANKING TOOL

We further evaluate the role of the brain encoder as a selection mechanism for decoded stimuli. Instead of relying on a single generated stimulus for each fMRI input, we sample multiple candidates and use the brain encoder to rank them against measured neural responses. Table 10 shows that increasing the number of candidate predictions consistently improves decoding performance.

Table 10: Effect of encoder-based selection across different number of predictions

Conditions	Low-Level				High-Level			
	PixCorr \uparrow	SSIM \uparrow	Alex(2) \uparrow	Alex(5) \uparrow	Incep \uparrow	CLIP \uparrow	Eff \downarrow	SwAV \downarrow
num of preds = 1	.104	.292	79.0%	90.1%	89.5%	90.8%	.729	.417
num of preds = 2	.105	.292	82.6%	91.7%	89.8%	88.7%	.733	.416
num of preds = 4	.120	.293	84.0%	93.5%	90.1%	91.5%	.725	.408
num of preds = 8	.133	.296	86.22%	93.96%	92.15%	92.03%	.706	.396

L EXPLANATIONS OF MIN-SNR LOSS WEIGHTING

At each diffusion timestep t , the effective signal-to-noise ratio is defined as

$$\text{SNR}_t = \frac{\bar{\alpha}_t}{1 - \bar{\alpha}_t},$$

where $\bar{\alpha}_t$ denotes the cumulative product of noise scheduling coefficients.

Without reweighting, high-SNR steps (early timesteps) tend to dominate the mean squared error (MSE) loss, while low-SNR steps (late timesteps) provide weaker gradients despite being more challenging and important for generation.

Ideally, the model should learn more from low-SNR noisy samples rather than overfitting to the easier, cleaner ones. Min-SNR weighting balances this trade-off by rescaling the per-timestep loss with

$$w_t = \frac{\min(\text{SNR}_t, \gamma)}{\text{SNR}_t},$$

where γ is a threshold hyperparameter (we set it to 5.0 in training).

M ROI ATTENTION MAP VISUALIZATION

To better interpret the ROI attention maps, we connect them to well-established functional regions. Because the Schaefer parcellation does not provide anatomical or functional labels for individual parcels, we assigned labels by mapping parcels to the labels available in NSD. A parcel was assigned to a given label if more than 50% of its vertices overlapped with that region. Using this mapping, we visualize the attention maps of the corresponding ROIs on generated images, tracking how their spatial influence evolves from noisy to clean across timesteps.

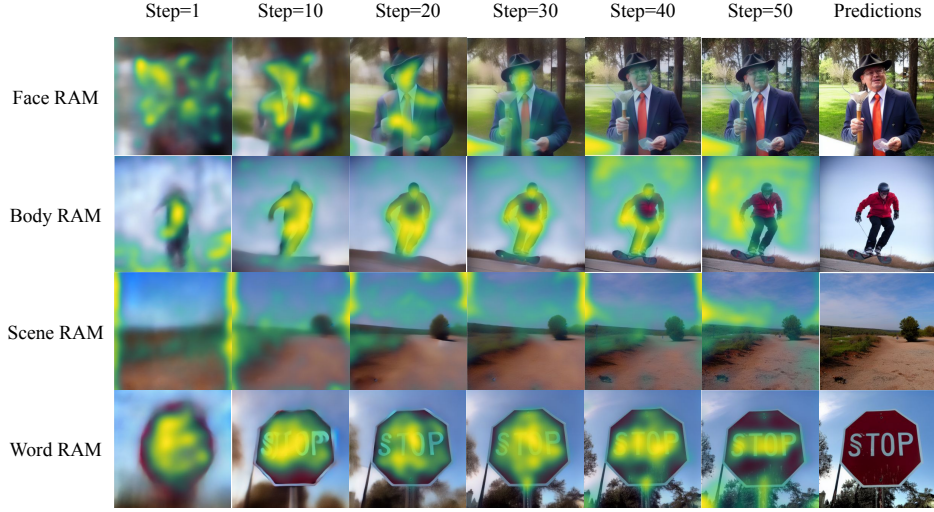


Figure 11: ROI attention map dynamics across generative timesteps

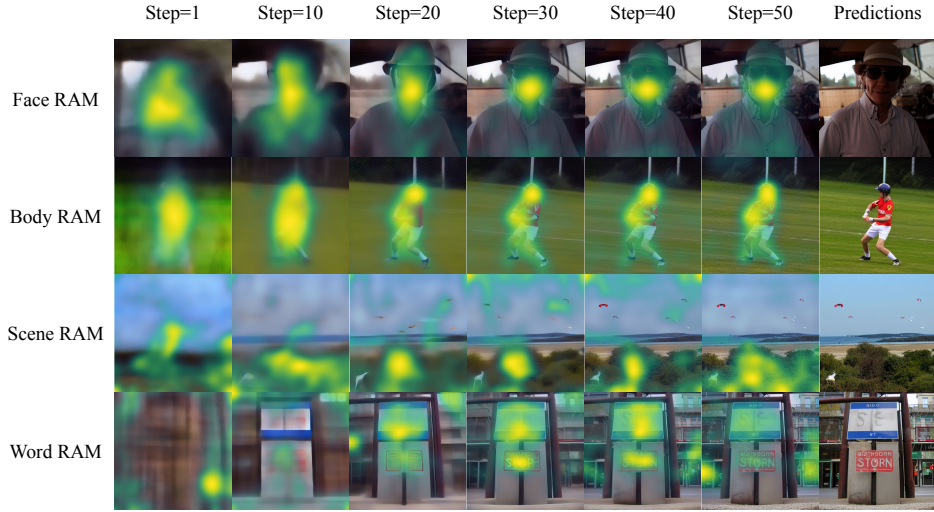


Figure 12: ROI attention map dynamics across generative timesteps

N CAUSAL PERTURBATION WITH BRAIN ROI MASKING

We present causal perturbation by masking out the related parcels of ROIs. Because the Schaefer parcellation does not provide anatomical or functional labels for individual parcels, we assigned labels by mapping parcels to the labels available in NSD. A parcel was assigned to a given label if more than 50% of its vertices overlapped with that region. In 200 parcels with high SNR, 103 parcels were labeled for subject 1. Among them, 50 parcels were labeled as low-level ROIs, including V1, V2, V3, and V4, while 53 parcels were annotated as Face, Body, Scene and Word ROIs.

Table 11: Effect of ROI masking (high-level vs. low-level) on model performance

Conditions	Low-Level				High-Level			
	PixCorr \uparrow	SSIM \uparrow	Alex(2) \uparrow	Alex(5) \uparrow	Incep \uparrow	CLIP \uparrow	Eff \downarrow	SwAV \downarrow
No Masking	.133	.296	86.22%	93.96%	92.15%	92.03%	.706	.396
LL ROI Masking	.119	.290	66.13%	78.38%	73.15%	74.20%	.891	.535
HL ROI Masking	.019	.289	55.42%	58.34%	50.70%	50.37%	.981	.641

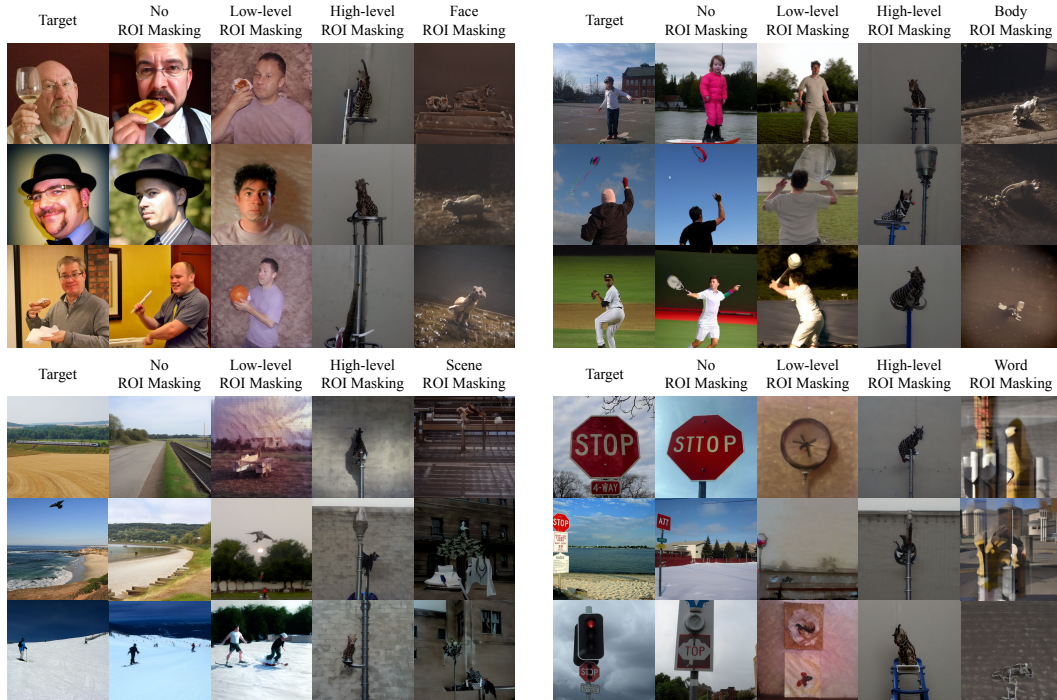


Figure 13: Visual Effect of brain masking on different ROIs

O EXAMPLES OF DECODED STIMULI ON NSD IMAGERY DATASET

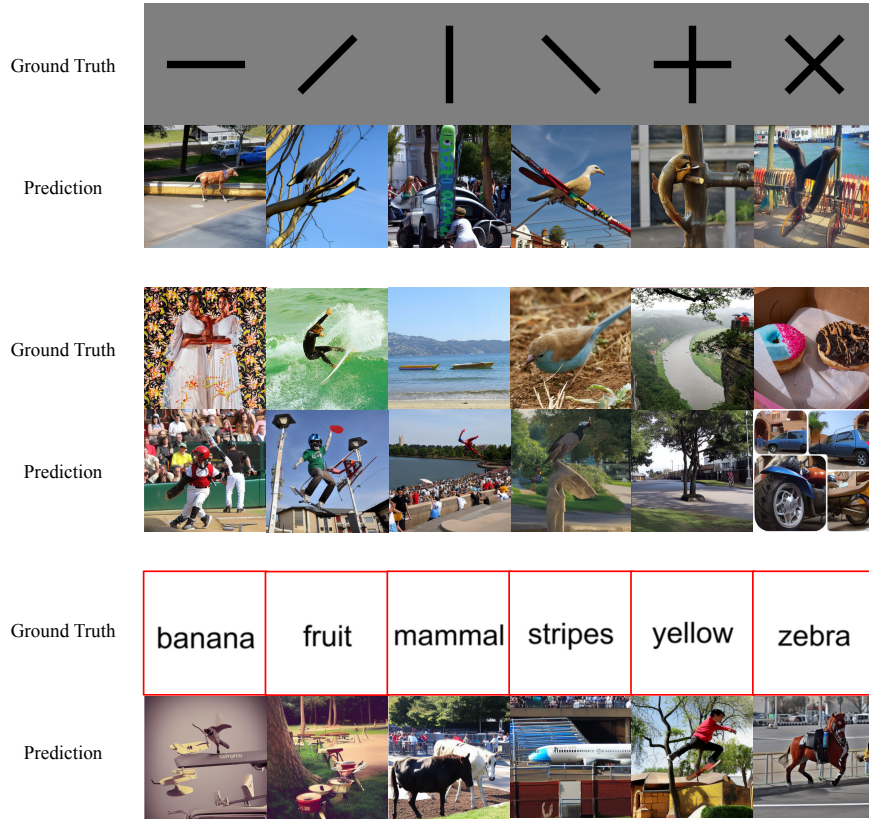


Figure 14: Best decoded examples on NSD-Imagery mental imagery task



Figure 15: Best decoded examples on NSD-Imagery vision task

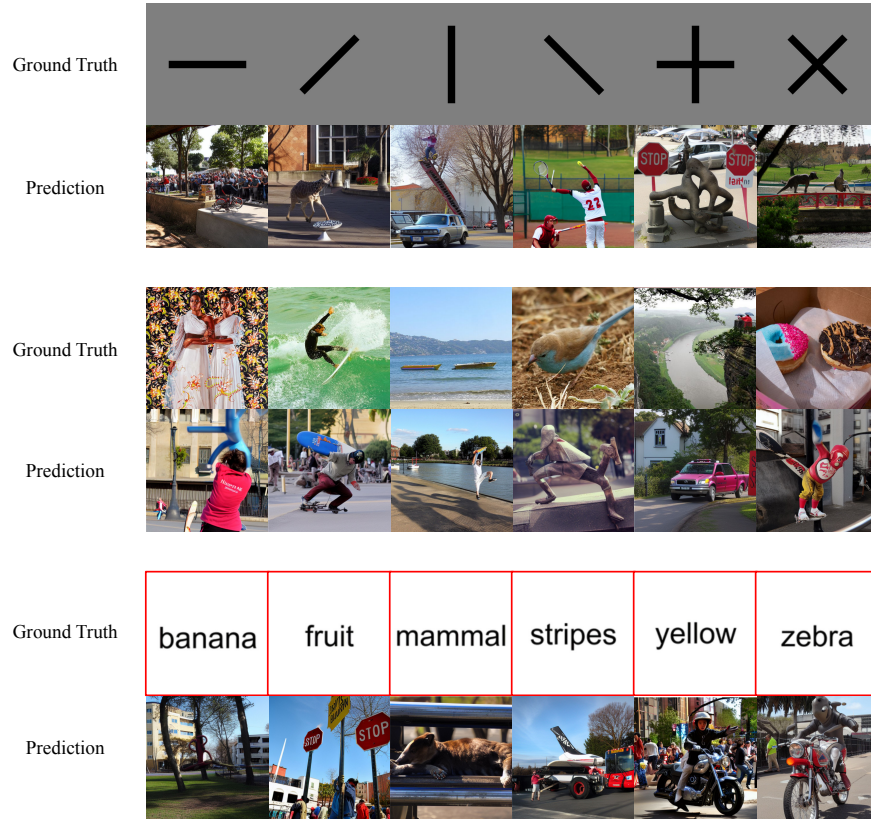


Figure 16: Worst decoded examples on NSD-Imagery mental imagery task



Figure 17: Worst decoded examples on NSD-Imagery vision task

P EXAMPLES OF DECODED STIMULI ON DEEPPRECON DATASET

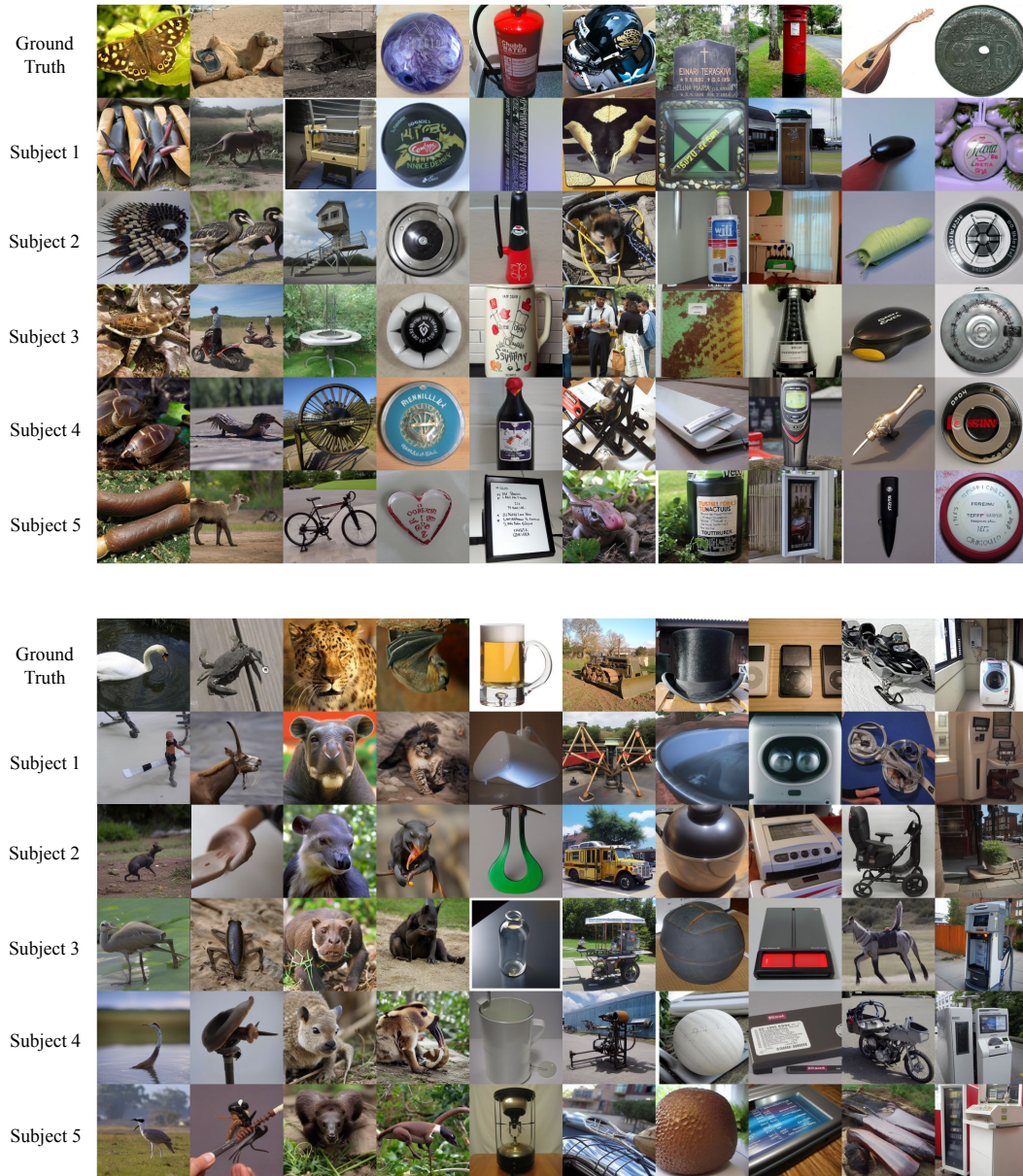


Figure 18: Decoded examples on Deeprecon natural image dataset

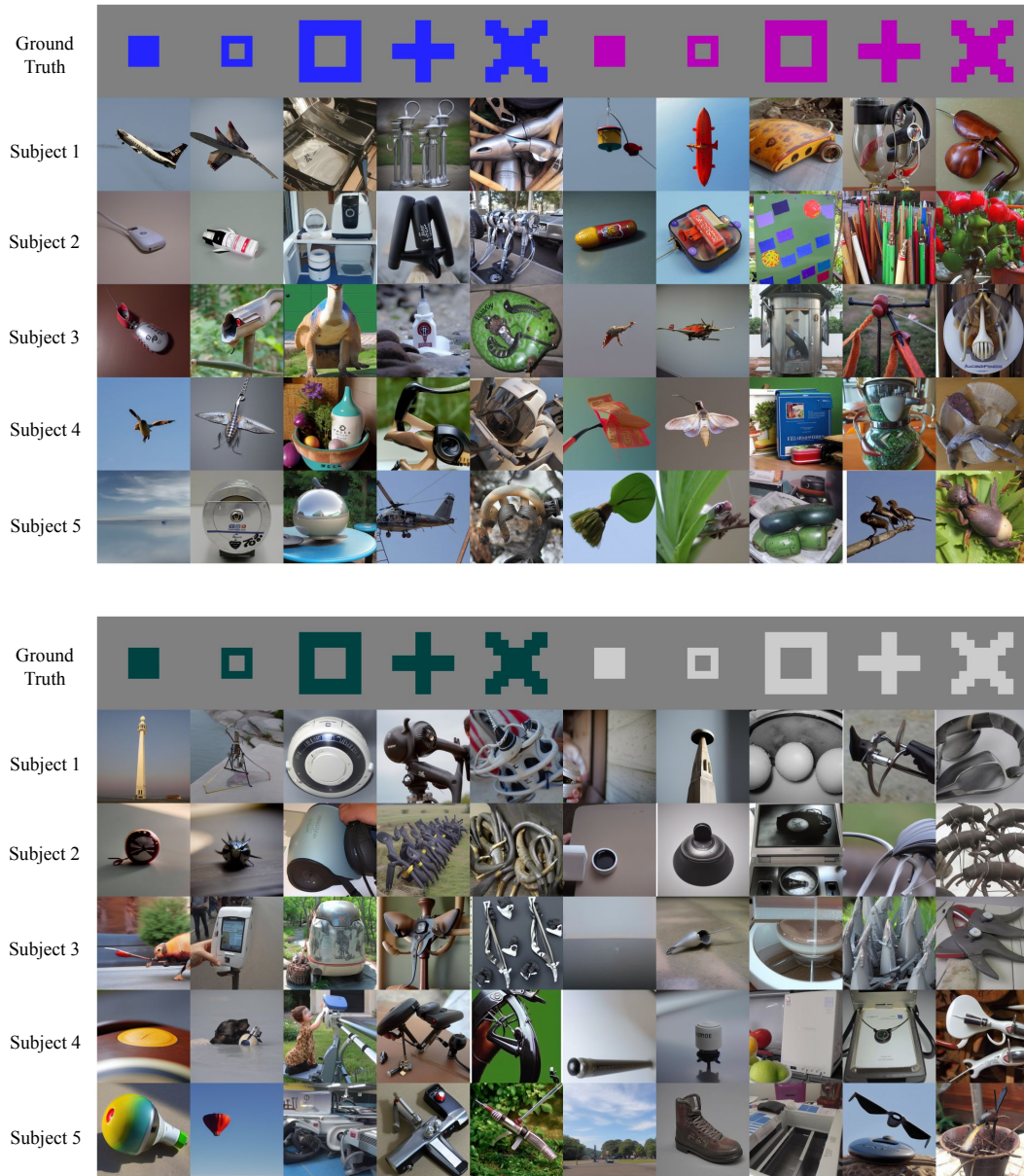


Figure 19: Decoded examples on Deeprecon artificial shape image dataset